

# Microscopic optical potentials for calcium isotopes\*

J. Rotureau,<sup>1</sup> P. Danielewicz,<sup>1,2</sup> G. Hagen,<sup>3,4</sup> G. R. Jansen,<sup>5,3</sup> and F. M. Nunes<sup>1,2</sup>

<sup>1</sup>*NSCL/FRIB Laboratory, Michigan State University, East Lansing, Michigan 48824, USA*

<sup>2</sup>*Department of Physics and Astronomy, Michigan State University, East Lansing, MI 48824-1321*

<sup>3</sup>*Physics Division, Oak Ridge National Laboratory, Oak Ridge, TN 37831, USA*

<sup>4</sup>*Department of Physics and Astronomy, University of Tennessee, Knoxville, TN 37996, USA*

<sup>5</sup>*National Center for Computational Sciences, Oak Ridge National Laboratory, Oak Ridge, TN 37831, USA*

We construct nucleonic microscopic optical potentials by combining the Green's function approach with the coupled-cluster method for  $^{40}\text{Ca}$  and  $^{48}\text{Ca}$ . For the computation of the ground-state of  $^{40}\text{Ca}$  and  $^{48}\text{Ca}$ , we use the coupled-cluster method in the singles-and-doubles approximation, while for the  $A = \pm 1$  nuclei we use particle-attached/removed equation-of-motion method truncated at two-particle-one-hole and one-particle-two-hole excitations, respectively. Our calculations are based on the chiral nucleon-nucleon and three-nucleon interaction  $\text{NNLO}_{\text{sat}}$ , which reproduces the charge radii of  $^{40}\text{Ca}$  and  $^{48}\text{Ca}$ , and the chiral nucleon-nucleon interaction  $\text{NNLO}_{\text{opt}}$ . In all cases considered here, we observe that the overall form of the neutron scattering cross section is reproduced for both interactions, but the imaginary part of the potential, which reflects the loss of flux in the elastic channel, is negligible. The latter points to neglected many-body correlations that would appear beyond the coupled-cluster truncation level considered in this work. We show that, by artificially increasing the parameter  $\eta$  in the Green's function, practical results can be further improved.

## I. INTRODUCTION

Nuclear reactions are the primary experimental tool to study atomic nuclei. With the recent progress in the development of rare-isotopes beams (RIBs), regions of the nuclear chart far from stability, that were previously out of reach, are now becoming accessible. More progress is expected, with future projects at RIB facilities, to explore systems far from stability [1–3]. In parallel to the progress on the experimental side, efforts should be pursued on the theoretical front to develop or extend reaction models to nuclei far from stability.

It is customary in reaction theory to reduce the many-body picture to a few-body one where only the most relevant degrees of freedom are retained [4]. In that case, one introduces effective interactions, the so-called optical potentials, between the clusters considered. Traditionally, these interactions have been constrained by data, particularly data on stable isotopes. Consequently, the use of these potentials to study exotic nuclei is unreliable and has uncontrolled uncertainties. In order to advance the field of nuclear reactions, it is then critical to connect the effective interaction to an underlying microscopic theory, so that extrapolations to exotic regions are better under control, together with rigorous assessment of uncertain-

ties.

Realistic ab-initio nuclear structure calculations based on nucleon-nucleon ( $NN$ ) and three-nucleon forces (3NFs) from chiral effective field theory [5–7] have now reached the point where reliable predictions for nuclei as heavy as  $^{100}\text{Sn}$  [8] can be made. This progress is due to the development of many-body methods that scale polynomially with system's size [9–19] and an ever increase of computational power. On the other hand, the ab-initio nuclear reaction community is behind in reached mass number, precision, and accuracy. There has been a lot of effort in developing microscopic reaction theories for light nuclei starting from realistic  $NN$  and 3NFs [20–30], while less so for medium-mass and heavy nuclei [31–35]. With upcoming experiments on rare isotopes in the medium- and heavy-mass region of the nuclear chart, it is important to develop ab-initio reaction theory that can make accurate predictions in these mass regions. It is the aim of this paper to take the first steps towards this goal.

In this paper, we will present ab-initio calculations of nucleon-nucleus optical potential for the doubly magic nuclei  $^{40}\text{Ca}$  and  $^{48}\text{Ca}$ . This work is the follow up of a previous study [35]. The optical potential (also known as the self-energy) enters the Dyson equation together with the one-body Green's function. Assuming some approximations for the self-energy, the standard way of obtaining the optical potential is to iterate the non-linear Dyson equation until a self-consistent solution is obtained. This is known as the self-consistent Green's function approach [11, 36–38]. Our approach differs from the self-consistent Green's function approach in that the optical potential is obtained directly by inverting the Dyson equation [35]. We calculate the single particle Green's function by combining the coupled-cluster method [9, 10, 39–43] with the Lanczos continued fraction method [27, 32, 35, 44–46] and employing a complex Berggren basis [47–51]. In this work we focus on the

---

\* This manuscript has been authored by UT-Battelle, LLC under Contract No. DE-AC05-00OR22725 with the U.S. Department of Energy. The United States Government retains and the publisher, by accepting the article for publication, acknowledges that the United States Government retains a non-exclusive, paid-up, irrevocable, world-wide license to publish or reproduce the published form of this manuscript, or allow others to do so, for United States Government purposes. The Department of Energy will provide public access to these results of federally sponsored research in accordance with the DOE Public Access Plan. (<http://energy.gov/downloads/doe-public-access-plan>).

chiral  $NN$  and  $NNN$  interaction  $NNLO_{\text{sat}}$ , which has been shown to produce accurate ground-state energies and charge radii from light to medium mass nuclei [52–56].

This paper is organized as follows. In Sec. II, we briefly revisit the formalism of the Green's function and the coupled-cluster method along with the Berggren basis. We start Sec. III by showing the convergence pattern of the optical potentials associated with the bound states in  $^{41}\text{Ca}$  and  $^{49}\text{Ca}$  and then, present cross sections results for the neutron elastic scattering on  $^{40}\text{Ca}$  and  $^{48}\text{Ca}$ . For comparison, we also show calculated elastic cross sections obtained with the  $NNLO_{\text{opt}}$  [57] interaction (also derived within the chiral-EFT approach) and the phenomenological Koning-Delaroché (KD) potential [58]. Finally, we conclude and discuss future possible applications in Sec. IV.

## II. FORMALISM

### A. The single-particle Green's function

Let us consider a nucleus with  $A$  nucleons. The single-particle Green's function for that nucleus has matrix elements

$$G(\alpha, \beta, E) = \langle \Psi_0 | a_\alpha \frac{1}{E - (H - E_{gs}^A) + i\eta} a_\beta^\dagger | \Psi_0 \rangle + \langle \Psi_0 | a_\beta^\dagger \frac{1}{E - (E_{gs}^A - H) - i\eta} a_\alpha | \Psi_0 \rangle, \quad (1)$$

where  $\alpha$  and  $\beta$  represent single-particle states, and  $|\Psi_0\rangle$  represents the ground state of the nucleus with energy  $E_{gs}^A$ . By definition, the parameter  $\eta$  is such that in the physical limit  $\eta \rightarrow 0^+$ . The operators  $a_\alpha^\dagger$  and  $a_\beta$  create and annihilate a nucleon in the single-particle state  $\alpha$  and  $\beta$ , respectively, and their labels are shorthands for the quantum numbers  $\alpha = (n, l, j, j_z, \tau_z)$ . Here,  $n, l, j, j_z, \tau_z$  label the radial quantum number, the orbital angular momentum, the total orbital momentum, its projection on the  $z$ -axis, and the isospin projection, respectively. The intrinsic Hamiltonian  $H$  reads

$$H = \sum_{i=1}^A \frac{\vec{p}_i^2}{2m} - \frac{\vec{P}^2}{2mA} + \sum_{i<j} V_{ij} + \sum_{i<j<k} V_{ijk}, \quad (2)$$

with  $\vec{p}_i$  the momentum of the nucleon  $i$  of mass  $m$  and  $\vec{P} = \sum_{i=1}^A \vec{p}_i$  the momentum associated with the center of mass motion. The terms  $V_{ij}$  and  $V_{ijk}$  are  $NN$  and  $3NFs$ , respectively. It is useful to rewrite the Hamiltonian as

$$H = \sum_{i=1}^A \frac{\vec{p}_i^2}{2m} \left(1 - \frac{1}{A}\right) + \sum_{i<j} \left(V_{ij} - \frac{\vec{p}_i \vec{p}_j}{mA}\right) + \sum_{i<j<k} V_{ijk}, \quad (3)$$

where one separates the one-body and two- (three-)body contributions. In the following, we work with the single-particle basis solutions of the Hartree-Fock (HF) potential generated by  $H$ . We recall here that the HF basis is

a good starting point for coupled-cluster calculations and that the HF Green's function denoted as  $G^{(0)}$  is a first order approximation to the Green's function (1). The Green's function fulfills the Dyson equation

$$G(\alpha, \beta, E) = G^{(0)}(\alpha, \beta, E) + \sum_{\gamma, \delta} G^{(0)}(\alpha, \gamma, E) \Sigma^*(\gamma, \delta, E) G(\delta, \beta, E). \quad (4)$$

Here,  $\Sigma^*(\gamma, \delta, E)$  is the self energy, which can be obtained from the inversion of Eq. (4):

$$\Sigma^*(E) = [G^{(0)}(E)]^{-1} - G^{-1}(E). \quad (5)$$

Finally, one obtains the optical potential as

$$\Sigma' \equiv \Sigma^* + U, \quad (6)$$

where  $U$  is the HF potential. For  $E \geq E_{gs}^A$ ,  $\Sigma'$  in Eq. (6) corresponds to the optical potential for the elastic scattering from the  $A$ -nucleon ground state [59, 60]. For  $E \leq E_{gs}^A$ ,  $\Sigma'$  has a discrete number of solutions which correspond to the bound states in the  $A+1$  nucleon system. The optical potential is non-local, energy-dependent and complex [60]; for  $E \geq E_{gs}^A$ , its imaginary component describes, by construction, the loss of flux due to absorption into channels other than the elastic channel.

In this paper, the optical potential is obtained by inverting the Dyson equation (4) after a direct computation of the Green's function (1) with the coupled-cluster method [43]. In the following, we present the main steps involved in the computation of the Green's function in our approach.

### B. Coupled-cluster approach for the Green's function

In this section we briefly show how we construct the Green's function following the coupled-cluster method. For a more detailed account, we refer the reader to [35, 41, 43]. In coupled-cluster theory, the ground state is represented as

$$|\Psi_0\rangle = e^T |\Phi_0\rangle, \quad (7)$$

where  $T$  denotes the cluster operator which gets expanded in the number of particle-hole excitations

$$T = T_1 + T_2 + \dots = \sum_{i,a} t_i^a a_a^\dagger a_i + \frac{1}{4} \sum_{ijab} t_{ij}^{ab} t_{ijab} a_a^\dagger a_b^\dagger a_j a_i + \dots \quad (8)$$

The operators  $T_1$  and  $T_2$  induce  $1p$ - $1h$  and  $2p$ - $2h$  excitations of the HF reference, respectively. Here, the single-particle states  $i, j, \dots$  refer to hole states occupied in the reference state  $|\Phi_0\rangle$  while  $a, b, \dots$  denote valence states above the reference state. In practice, the expansion (8) is truncated. In the coupled-cluster with singles and doubles (CCSD) all operators  $T_i$  beyond  $i = 2$  are neglected.

One can show that the CCSD ground state is an eigenstate of the similarity-transformed Hamiltonian  $\bar{H} \equiv e^{-T} H e^T$  in the space of  $0p-0h$ ,  $1p-1h$ ,  $2p-2h$  configurations. Note that the transformed Hamiltonian is not Hermitian because the operator  $e^T$  is not unitary. As a consequence,  $\bar{H}$  has left- and right-eigenvectors which constitute a bi-orthogonal basis with the following completeness relation

$$\sum_i |\Phi_{i,R}\rangle \langle \Phi_{i,L}| = \hat{1}, \quad (9)$$

where the right ground state  $|\Phi_{0,R}\rangle$  is the reference state  $|\Phi_0\rangle$ , while the left ground-state is given by  $\langle \Phi_{0,L}| = \langle \Phi_0|(1 + \Lambda)$  with  $\Lambda$  a linear combination of particle-hole de-excitation operators.

Using the ground state of the similarity-transformed Hamiltonian  $\bar{H}$ , we can now write the coupled-cluster Green's function  $G^{CC}$  as

$$\begin{aligned} G^{CC}(\alpha, \beta, E) \equiv & \\ & \langle \Phi_{0,L} | \bar{a}_\alpha \frac{1}{E - (\bar{H} - E_{gs}^A) + i\eta} \bar{a}_\beta^\dagger | \Phi_0 \rangle \\ & + \langle \Phi_{0,L} | \bar{a}_\beta^\dagger \frac{1}{E - (E_{gs}^A - \bar{H}) - i\eta} \bar{a}_\alpha | \Phi_0 \rangle. \end{aligned} \quad (10)$$

In the expression above,  $\bar{a}_\alpha = e^{-T} a_\alpha e^T$  and  $\bar{a}_\beta^\dagger = e^{-T} a_\beta^\dagger e^T$  are the similarity-transformed annihilation and creation operators, respectively. We note that the truncation of the cluster operator  $T$  is reflected in the expression of the coupled-cluster Green's function (10) and, if all excitations up to  $Ap-Ah$  were taken into account in the expansion (8), the Green's function (10) would be exact and identical to (1). In principle, the Green's function could be obtained by inserting completeness relations into (10), with the solutions of the the  $A \pm 1$  systems obtained with the particle-attached equation-of-motion (PA-EOM) and particle-removed equation-of-motion (PR-EOM) coupled-cluster methods [61]. However, in practice, this approach is difficult to pursue as the sum over all states also involves eigenstates in the continuum. To bypass this issue, we use the Lanczos continued fraction technique [27, 32, 35, 44–46] for the computation of the the Green's function Eq. (10).

### C. Berggren basis

Our goal is to compute the optical potential for elastic scattering at arbitrary energies. However, as  $\eta \rightarrow 0^+$ , the coupled-cluster Greens' function in Eq. (10) has poles at energies  $E = (E_i^{A+1} - E_{gs}^A)$  (with  $E_i^{A+1}$  the eigenvalues of the  $A+1$  system), which make the numerical calculation unstable.

In order to bypass this issue, we consider, as we did in [35], an analytic continuation of the Green's function in the complex-energy plane. This is achieved by working in

the complex Berggren basis (generated by the HF potential), which includes bound-, resonant, and discretized non-resonant continuum states [47–51]. In our previous work we considered only  $NN$  interactions, while in this work we also consider 3NFs, and the transformation of the Hamiltonian to the Berggren basis is thus much more involved. In order to obtain the Berggren HF basis, and transform the Hamiltonian with 3NFs to this basis, we follow the numerically efficient procedure outlined in Ref. [62]. As a consequence, the many-body spectrum for the  $A + 1$  ( $A - 1$ ) systems obtained with the PA-EOM (PR-EOM) is composed of bound, resonant and complex-continuum states *i.e.* the poles of the analytically continued Green's function have either a negative real or complex energy. In that case, the Green's function matrix elements for  $E \geq 0$  smoothly converge to a finite value as  $\eta \rightarrow 0^+$ .

In order to fulfill the Berggren completeness [47], the complex-continuum single-particle states must be located along a contour  $L^+$  in the fourth quadrant of the complex momentum plane, below the resonant single-particle states. According to the Cauchy theorem, the form of the contour  $L^+$  is not important, as long as all resonant states lie between the contour and the real momentum axis. The Berggren completeness then reads

$$\sum_i |u_i\rangle \langle \tilde{u}_i| + \int_{L^+} dk |u(k)\rangle \langle \tilde{u}(k)| = \hat{1}, \quad (11)$$

where  $|u_i\rangle$  are discrete states corresponding to bound and resonant solutions of the single-particle potential, and  $|u(k)\rangle$  are complex-energy scattering states along the complex-contour  $L^+$ . In practice, the integral along the complex continuum is discretized yielding a finite discrete basis set.

## III. RESULTS

We present here applications of the coupled-cluster Green's function approach for  $^{40}\text{Ca}$  and  $^{48}\text{Ca}$ . We show results for the bound states in  $^{41}\text{Ca}$  and  $^{49}\text{Ca}$  as well as for the neutron elastic scattering.

Calculations are performed using the NNLO<sub>sat</sub> chiral interaction [52] which reproduces the binding energy and charge radius for both systems [53, 54]. All results reported here are obtained from coupled-cluster calculations truncated at the CCSD level, while the PA-EOM and PR-EOM Lanczos vectors have been truncated at the 2p-1h and 1p-2h excitation level, respectively.

We first perform HF calculations in a single-particle basis that employs a mixed representation of harmonic oscillator and Berggren states. More precisely, to calculate a neutron-target optical potential in the  $(l, j)$  channel, we use only Berggren states for the  $(l, j)$  neutron partial wave, whereas the rest are taken as harmonic oscillator shells. We include all harmonic oscillator shells such that  $2n + l \leq N_{max}$ . We checked that the results do not require a special treatment of the continuum in the

other partial waves. The Berggren states are introduced as a discretized set of  $N_{berg} = 50$  states along a contour in the complex-k plane up to  $k_{max} = 4fm^{-1}$ . This is sufficiently precise to ensure that results are independent of the form of the contour in the complex-plane.

The  $NNLO_{sat}$  interaction includes a two-body and three-body terms. Let us denote  $N_2$  and  $N_3$  the cut-offs of the interaction terms defined respectively as the maximum number of quanta allowed in the relative motion of two nucleons and three nucleons. In all calculations here, we always take  $N_2 = N_{max}$  and  $N_3$  is taken equal to  $N_{max}$ , except for the most extensive calculations considered here where  $N_{max} = 14$  and  $N_3 = 16$ . Moreover, the three-nucleon forces are truncated at the normal-ordered two-body level in the HF basis [62]. The harmonic oscillator frequency is kept fixed at  $\hbar\omega = 16$  MeV.

To provide perspective, we also show results for the neutron elastic scattering obtained with the chiral  $NN$  interaction  $NNLO_{opt}$  interaction [57]. In that case, the calculations were carried out for  $N_{max} = 14$  with the harmonic oscillator frequency  $\hbar\omega=20$  MeV.

We begin by studying the numerical convergence for the bound states and the associated optical potentials in  $^{41}\text{Ca}$  and  $^{49}\text{Ca}$ .

### A. Convergence for bound states

The energy for the bound states in  $^{41}\text{Ca}$  and  $^{49}\text{Ca}$ , solutions of the PA-EOM CCSD equations, are shown in Tab. I as a function of  $N_{max}$ . For both nuclei, there are only three bound states supported by the  $NNLO_{sat}$  Hamiltonian. As expected, the convergence pattern is slower for the higher-energy states. Specifically, for  $^{41}\text{Ca}$ , the difference between the energies obtained for  $(N_{max}, N_3)=(14,14)$  and  $(14,16)$  is  $\sim 220$  keV in the case of the ground-state, whereas it is  $\sim 350$  keV in the case of the  $J^\pi = 1/2^-$  second excited state. For  $^{49}\text{Ca}$ , the difference is  $\sim 210$  keV for the ground state and  $\sim 420$  keV for the  $J^\pi = 5/2^-$  excited state.

Even though the absolute binding energy is underestimated in the CCSD approximation, when compared to experiment (for  $^{40}\text{Ca}$  we obtain a binding energy of 299.28 MeV for  $(N_{max}, N_3) = (14, 16)$ , whereas the experimental value is 342.05 MeV), the neutron separation energies are consistently within 600 keV of the experimental values. By including both perturbative triples excitations and perturbative estimates for the neglected residual 3NFs (3NF terms beyond the normal-ordered two-body approximation), a good agreement with experimental binding energies can be obtained for  $^{40,48}\text{Ca}$  [53].

We show for illustration in Fig. 1, the converging pattern of the real part of the radial (diagonal) optical potential for the three bound states in  $^{41}\text{Ca}$ . By construction, the calculated eigenenergies of these potentials are equal to the bound states energies in Tab. I when using the

	$N_{max}$	$E(7/2^-)$	$E(3/2^-)$	$E(1/2^-)$
$^{41}\text{Ca}$	12	-7.35	-3.47	-1.31
	14	-7.62	-3.87	-1.80
	14 ( $N_3=16$ )	-7.84	-4.07	-2.15
	Exp	-8.36	-6.42	-4.74
$^{49}\text{Ca}$		$E(3/2^-)$	$E(1/2^-)$	$E(5/2^-)$
	12	-3.88	-2.025	-0.37
	14	-4.35	-2.40	-1.00
	14 ( $N_3=16$ )	-4.56	-2.45	-1.42
Exp		-5.14	-3.12	-1.56

TABLE I. PA-EOM CCSD energies (in MeV) for bound states in  $^{41}\text{Ca}$  and  $^{49}\text{Ca}$  calculated with the chiral  $NNLO_{sat}$  interaction as a function of  $N_{max}$ .

effective mass  $m A/(A-1)$  instead of the actual reduced mass  $m (A-1)/A$ . This can be traced to Eq. (3) where the effective mass associated with the kinetic operator is equal to  $m A/(A-1)$ .

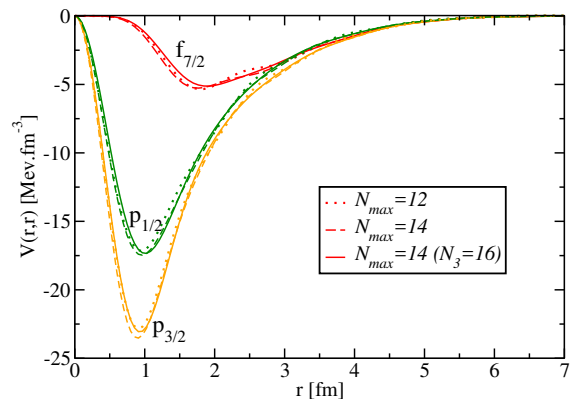


FIG. 1. (Color online) Real part of the radial (diagonal) optical potential for the bound states in  $^{41}\text{Ca}$ , calculated with the  $NNLO_{sat}$  interaction. Results are shown for the  $f_{7/2}$ ,  $p_{3/2}$  and  $p_{1/2}$  neutron partial waves and for several values of  $N_{max}$ .

In the following, we study the convergence pattern for the neutron elastic scattering on  $^{40}\text{Ca}$  and  $^{48}\text{Ca}$  and the corresponding optical potentials.

### B. Convergence for scattering states

We now turn our attention to the neutron elastic scattering on  $^{40}\text{Ca}$  and  $^{48}\text{Ca}$ . For each partial wave, the scattering phase shift is calculated from the single-particle Schrödinger equation using the optical potential in Eq. (6) and the reduced mass  $m (A-1)/A$ . Few comments are in order here. Since the calculations of the optical potential are performed using the laboratory

$N_{max}$		$\delta_{s_{1/2}}$	$\delta_{p_{1/2}}$	$\delta_{p_{3/2}}$	$\delta_{d_{3/2}}$	$\delta_{d_{5/2}}$
$^{40}\text{Ca}$	(E=5.17 MeV)					
	12	-93	80	89	1	-99
	14	-75	77	88	18	-86
	14 ( $N_3=16$ )	-68	78	89	35	-86
$N_{max}$		$\delta_{s_{1/2}}$	$\delta_{p_{1/2}}$	$\delta_{p_{3/2}}$	$\delta_{g_{7/2}}$	$\delta_{g_{9/2}}$
$^{48}\text{Ca}$	(E=7.81 MeV)					
	12	-93	55	62	13	-10
	14	-83	53	65	22	-10
	14 ( $N_3=16$ )	-85	53	69	37	-11

TABLE II. Real part (in degrees) of the neutron scattering phase shifts calculated with the  $\text{NNLO}_{\text{sat}}$  Hamiltonian at 5.17 MeV for  $^{40}\text{Ca}$  and, 7.81 MeV for  $^{48}\text{Ca}$ . Results are shown as a function of  $N_{max}$ .

coordinates (the Hamiltonian  $H$  in Eq. (3) is defined with these coordinates), the optical potential in Eq. (6) is obtained in these coordinates and not in the relative neutron-target coordinate. However, we will assume here that we can identify the potential in the relative coordinate with the potential calculated with Eq. (6). The error associated with this approximation gets smaller as the mass of the nuclei involved increases [63].

We show in Tab. II the real part of the phase shifts for a few partial waves for each isotope, at a given scattering beam energy. The results are shown as a function of  $N_{max}$  for neutron scattering at  $E=5.17$  MeV on  $^{40}\text{Ca}$ , and at  $E=7.81$  MeV on  $^{48}\text{Ca}$ . One can see that some of the phase shifts in Tab. II are well converged whereas there are variations with the model-space sizes in other cases. For instance, convergence is reached for all but the  $s_{1/2}$  and  $d_{3/2}$  partial waves for the neutron scattering on  $^{40}\text{Ca}$  at 5.17 MeV. For the neutron scattering on  $^{48}\text{Ca}$  at 7.81 MeV, the phase shifts are converged for all but the  $g_{7/2}$  partial wave. This difference in the convergence pattern is not unexpected and we have found that the partial waves for which the phase shifts converge slower correspond to those that exhibit a stronger energy dependence around the energy of interest.

For both systems, the phase shifts should have a finite imaginary part which reflects the loss of flux in the elastic channel. For instance, in the case of  $^{40}\text{Ca}$  at  $E=5.17$  MeV, there is a potential absorption due to excitation of  $^{40}\text{Ca}$  to either its first excited state  $E(0^+) = 3.35$  MeV or second excited state  $E(3^-) = 3.74$  MeV. However, calculations yield a negligible value for the absorption in all partial waves. We will return to this point in the next section.

Next, we obtain elastic angular distributions by summing the contribution from each partial wave. We show in Figs. 2 and 3 the angular distribution for  $^{40}\text{Ca}(n,n)^{40}\text{Ca}$  at 5.17 MeV and  $^{48}\text{Ca}(n,n)^{48}\text{Ca}$  at 7.81 MeV, as a function of  $N_{max}$ . We find that the inclusion of partial waves with angular momentum  $L \leq 5$  and  $L \leq 6$  is sufficient for  $^{40}\text{Ca}$  and  $^{48}\text{Ca}$ , respectively, the contribution of partial waves with higher  $L$  being neg-

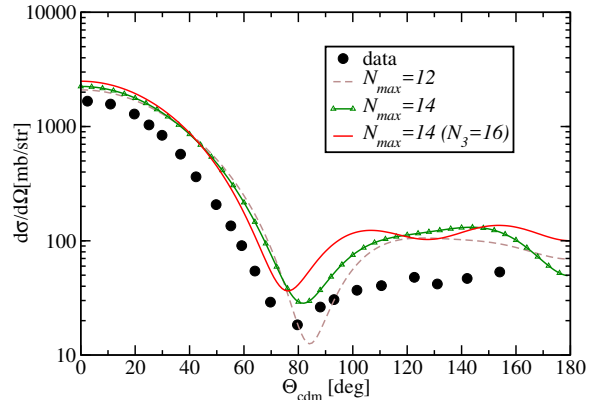


FIG. 2. (Color online) Differential elastic cross section for  $^{40}\text{Ca}(n,n)^{40}\text{Ca}$  at 5.17 MeV, calculated with the  $\text{NNLO}_{\text{sat}}$  interaction, as a function of  $N_{max}$ . Data points are taken from [58].

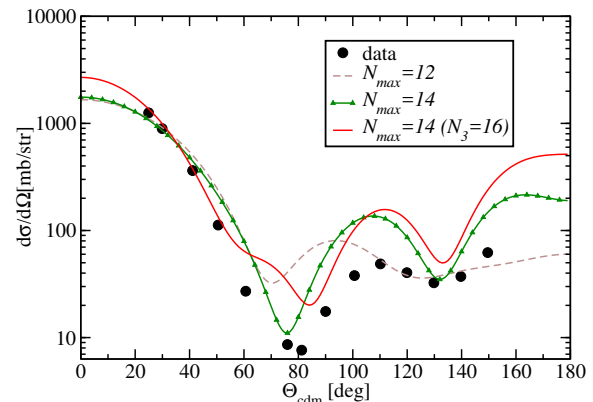


FIG. 3. (Color online) Differential elastic cross section for  $^{48}\text{Ca}(n,n)^{48}\text{Ca}$  at 7.81 MeV, with the  $\text{NNLO}_{\text{sat}}$  interaction, as a function of  $N_{max}$ . Data points are taken from [58].

ligible. All scattering phase shifts other than the ones shown in Tab. II have converged with respect to  $N_{max}$ . The variations around the first minimum are significant and are a consequence of the convergence pattern of the scattering phase shifts with  $N_{max}$ . We understand then that the calculated cross sections will contain an error due to the model-space truncation. Note that however, for  $(N_{max}, N_3) = (14, 16)$ , the calculated distribution for  $^{48}\text{Ca}(n,n)^{48}\text{Ca}$  is already in excellent agreement with the data at lower angles where the differential cross section is the largest.

Finally, we show for illustration in Fig. 4, the converging pattern of the real (diagonal) part of the op-

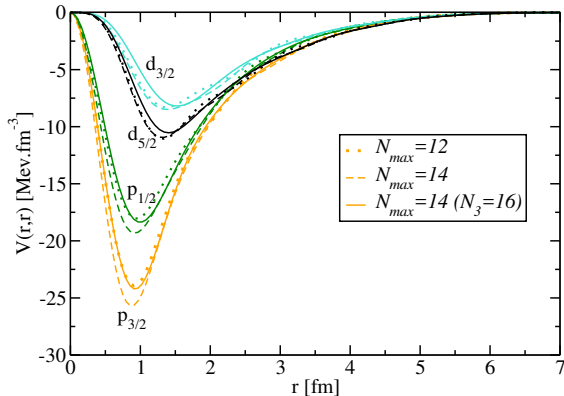


FIG. 4. (Color online) Real part of the diagonal optical potential for  $^{40}\text{Ca}(n,n)^{40}\text{Ca}$  at  $E=5.17$  MeV, calculated with the  $\text{NNLO}_{\text{sat}}$  interaction, as a function of  $N_{\text{max}}$ . Results are shown for the neutron  $p_{1/2}, p_{3/2}, d_{3/2}, d_{5/2}$  partial waves.

tical potentials in the neutron  $p, d$  partial waves for  $^{40}\text{Ca}(n,n)^{40}\text{Ca}$  at 5.17 MeV as a function of  $N_{\text{max}}$ . All corresponding phase shifts have converged excepted for the  $d_{3/2}$  partial wave (cf. Tab. II).

### C. Results with finite values of $\eta$

As we mentioned previously, the calculated optical potentials for neutron scattering on  $^{40}\text{Ca}$  at  $E=5.17$  MeV and  $^{48}\text{Ca}$  at 7.81 MeV both have negligible absorption.

In order to understand this feature better, let us consider in more details the scattering on  $^{40}\text{Ca}$  at 5.17 MeV. In that case, there is enough energy for the scattered neutron to excite the target ( $^{40}\text{Ca}$  in its ground state) to its two first excited states located at  $E(0^+) = 3.35$  MeV and  $E(3^-) = 3.74$  MeV. However the  $0^+$  excited state (which is known to have significant  $4p - 4h$  components) is not properly captured in the EOM-CCSD approximation: its calculated energy is at 15.98 MeV above the ground state. On the other hand, the energy of the second excited state is well reproduced at the EOM-CCSD level with  $E_{\text{EOM-CCSD}}(3^-) = 3.94$  MeV. Consequently, only potential excitation to the second excited state could in principle be accounted for. The fact that the calculated absorption is nevertheless negligible implies that the CCSD and PA-EOM wave functions are not sufficiently correlated. In other words, correlations beyond the singles and doubles truncation level are needed to account for the absorption due to target excitation. The situation is similar for the scattering off of  $^{48}\text{Ca}$ : in that case, the position of the first excited state  $E(2^+) = 3.83$  MeV is fairly well reproduced at the EOM-CCSD level with  $E_{\text{EOM-CCSD}}(2^+) = 4.65$  MeV, but the calculated ab-

sorption is still negligible pointing out again to a lack of correlations in the CCSD and PA-EOM wavefunctions.

We should also note that the formation of a compound nucleus will contribute to flux removal from the elastic channel. However, again, at that level of truncation, this cannot be accounted for since the compound states consist of a high number of particle-hole excitations and are usually described by stochastic approaches [64].

We have seen here that one would need to consider excitations beyond the singles and doubles excitations to describe the absorption seen in nature. However, a cheaper solution may be provided by artificially considering finite values of  $\eta$  instead of taking the limit  $\eta \rightarrow 0^+$  (see Eq. 10). In the following, we explore the impact of using finite  $\eta$  values on the optical potential and the scattering phase shift.

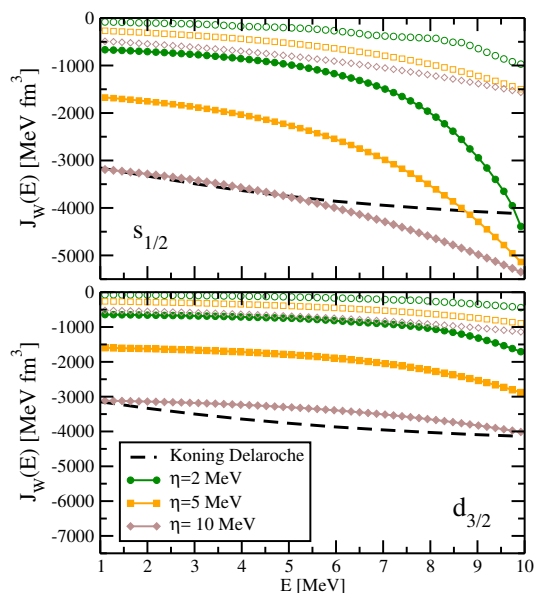


FIG. 5. (Color online) Volume integral  $J_W(E)$  of the imaginary part of the neutron optical potential in the  $s_{1/2}$  (upper panel) and  $d_{3/2}$  (lower panel) partial wave for  $^{40}\text{Ca}(n,n)^{40}\text{Ca}$  as a function of energy  $E$ . Results are shown for the  $\text{NNLO}_{\text{sat}}$  (symbols with lines) and  $\text{NNLO}_{\text{opt}}$  (symbols without lines) interactions at  $\eta = 2, 5, 10$  MeV. Results for the KD potential are also shown for comparison.

We show in Fig. 5 the imaginary volume integral  $J_W^l(E)$ ,

$$J_W^l(E) = 4\pi \int dr r^2 \int dr' r'^2 \text{Im} \Sigma_l^l(r, r'; E) \quad (12)$$

of the optical potential for  $^{40}\text{Ca}(n,n)^{40}\text{Ca}$  in the  $s_{1/2}$  and  $d_{3/2}$  partial waves with  $\eta = 2, 5, 10$  MeV. Results are shown for the  $\text{NNLO}_{\text{sat}}$  and  $\text{NNLO}_{\text{opt}}$  interactions and the KD potential. While these quantities are not observables, the comparison with the integral of the KD potential is instructive (see Fig. 5) and underscores the lack of

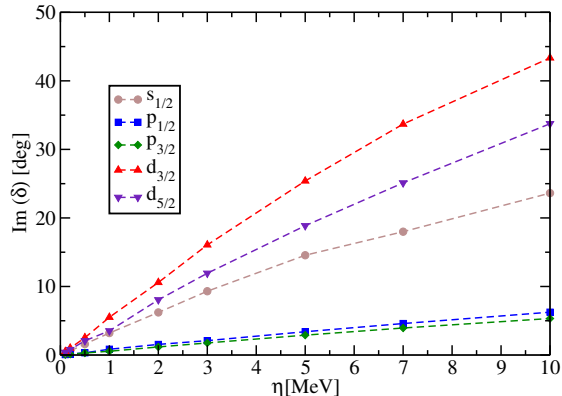


FIG. 6. (Color online) Imaginary part of the phase shift in the  $spd$  partial waves for  $^{40}\text{Ca}(n,n)^{40}\text{Ca}$  at 5.17 MeV as a function of  $\eta$ .

significant absorption of the potential calculated with the coupled-cluster Green's function at the singles and doubles approximation level. Obviously, increasing the value of  $\eta$ , increases the value of the integrals (in modulus) and consequently the neutron absorption in the scattering reaction. This is further illustrated in Fig. 6 where we show the imaginary part of the scattering phase shifts for  $^{40}\text{Ca}(n,n)^{40}\text{Ca}$  at 5.17 MeV as a function of  $\eta$ . For  $\eta=0$  MeV, all phase shifts have a vanishing imaginary part and as  $\eta$  increases, the imaginary parts increase more or less depending on the partial wave considered. If we were interested in reproducing the volume integral of the KD potential at 5.17 MeV in the  $s_{1/2}$  partial wave, one would choose a value of  $\eta \sim 10$  MeV (see Fig. 5).

In the following section, we show results for the elastic cross section on  $^{40}\text{Ca}$  and  $^{48}\text{Ca}$  with increasing absorption by using finite values of  $\eta$ .

#### D. Results for elastic scattering

We now discuss predictions for the elastic cross section when considering values of  $\eta = 0, 2, 5$  MeV, for  $^{40}\text{Ca}$  and  $^{48}\text{Ca}$ . All calculations presented in this section correspond to the largest model space discussed in the previous section namely  $N_{max} = 14$  and  $N_3 = 16$ .

The calculated differential elastic cross sections for neutron scattering on  $^{40}\text{Ca}$  at  $E=5.17$  MeV and  $E=6.4$  MeV are shown in Fig. 7 and Fig. 8 respectively. The top (bottom) panel corresponds to the results using the  $\text{NNLO}_{\text{sat}}$  ( $\text{NNLO}_{\text{opt}}$ ) interaction. For comparison, we also show the angular distributions obtained with the phenomenological KD potential, and also the measured cross sections (errors on the data are smaller than the symbols). As expected, when  $\eta$  increases, the elastic scat-

tering cross section decreases with a more pronounced (relative) reduction at larger angles. Moreover, the agreement with data improves as  $\eta$  increases. The level of disagreement between the experimental data and the result obtained with KD is an illustration of the level of accuracy that can be expected from a phenomenological global interaction.

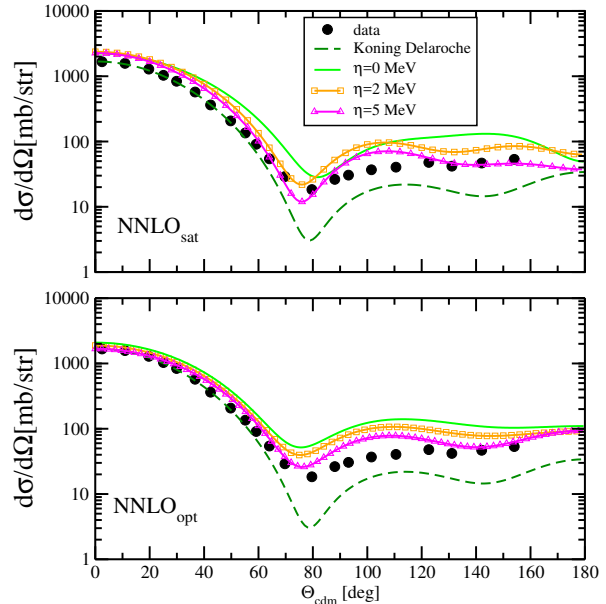


FIG. 7. (Color online) Differential elastic cross section for  $^{40}\text{Ca}(n,n)^{40}\text{Ca}$  at 5.17 MeV calculated with the  $\text{NNLO}_{\text{sat}}$  (top) and  $\text{NNLO}_{\text{opt}}$  (bottom) interactions. Calculations are shown for  $\eta = 0, 2, 5$  MeV. Results obtained using the KD potential are shown for comparison. Data points are taken from [58].

Next, we show predictions for neutron elastic scattering on  $^{48}\text{Ca}$  at  $E=4$  MeV (Fig. 9) and  $E=7.81$  MeV (Fig. 10). There is no data available for the neutron elastic scattering at 4 MeV, but we chose to include it in our study to show that the general behavior of increasing absorption is the same independently of the scattering energy and the target system. As for  $^{40}\text{Ca}$ , it is also clear that when including  $\eta$  as a fine-tuning parameter we can improve the agreement with data. Note that even at  $\eta = 0$  MeV, the calculated distribution for  $\text{NNLO}_{\text{sat}}$  in Fig. 10 is in excellent agreement with the data at smaller angles where the differential cross section is the largest. The same characteristics shown for  $^{40}\text{Ca}$  are present in  $^{48}\text{Ca}$  case, namely the cross section is not strongly dependent on  $\eta$  at small angles, while at larger angles the cross section is significantly reduced with increasing  $\eta$ . Moreover, for both nuclei, the results show a sensitivity of the distributions to the employed Hamiltonian.

An encouraging result of our calculations is that, within the energy range considered in this work, fine-

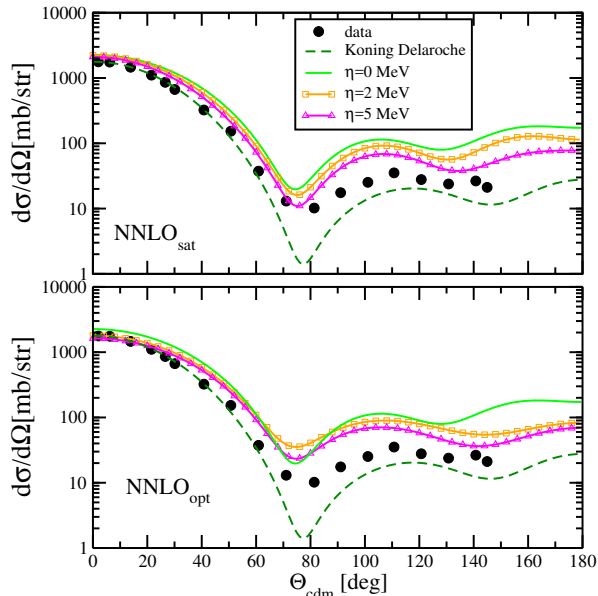


FIG. 8. (Color online) Differential elastic cross section for  $^{40}\text{Ca}(n,n)^{40}\text{Ca}$  at 6.34 MeV calculated with the  $\text{NNLO}_{\text{sat}}$  (top) and  $\text{NNLO}_{\text{opt}}$  (bottom) interactions. Calculations are shown for  $\eta = 0, 2, 5$  MeV. Results obtained using the KD potential are shown for comparison. Data points are taken from [58].

tuning  $\eta$  allows us to improve the description of neutron elastic scattering for both  $^{40}\text{Ca}$  and  $^{48}\text{Ca}$ . The value of  $\eta$  we use should not be interpreted as the effective width of the states, but rather as a means to compensate for the truncations inherent to our approach.

A	E (MeV)	$\eta = 0$ MeV	$\eta = 2$ MeV	$\eta = 5$ MeV	KD
40	5.17	229(12)	195(13)	166(12)	108
	6.3	195(3)	169(10)	144(9)	96
48	7.81	182 (32)	159(13)	139 (12)	88

TABLE III. Total elastic cross sections (in b) calculated with the  $\text{NNLO}_{\text{sat}}$  interaction for  $^{40}\text{Ca}$  and  $^{48}\text{Ca}$ . Results are shown for  $\eta = 0, 2, 5$  MeV. For each case, we assign an error defined as the difference between the calculated cross section obtained with  $(N_{\text{max}}, N_3) = (14, 16)$  and  $(N_{\text{max}}, N_3) = (14, 14)$ . Results obtained with the KD potential are shown for comparison.

Finally in Tab. III, we show the total elastic cross sections for both isotopes and energies, as a function of  $\eta$ . These were obtained by integrating the differential cross sections over angle. We only show the value for  $\text{NNLO}_{\text{sat}}$  (the same features appear when using  $\text{NNLO}_{\text{opt}}$ ). We also include an error based on the model space truncation: we assign an error as being the difference between the total cross section obtained with  $(N_{\text{max}}, N_3 =$

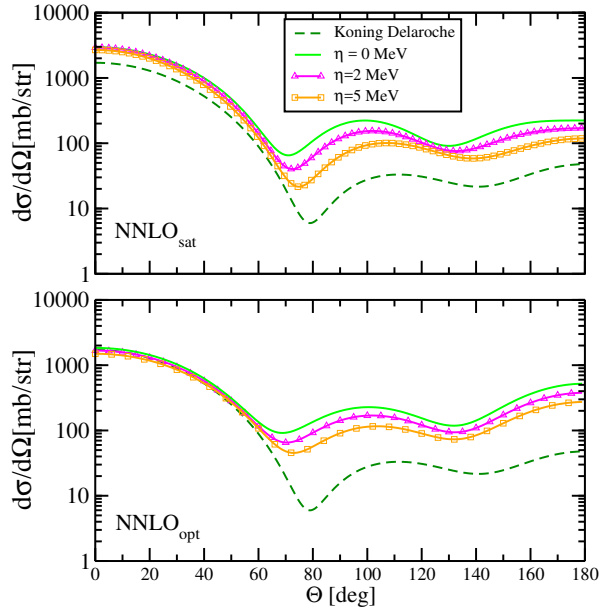


FIG. 9. (Color online) Differential elastic cross section for  $^{48}\text{Ca}(n,n)^{48}\text{Ca}$  at 4.00 MeV calculated with the  $\text{NNLO}_{\text{sat}}$  (top) and  $\text{NNLO}_{\text{opt}}$  (bottom) interactions. Calculations are shown for  $\eta = 0, 2, 5$  MeV. Results obtained using the KD potential are shown for comparison.

(14, 16) and that for  $(N_{\text{max}}, N_3) = (14, 16)$ . In the last column, we show the results using the phenomenological interaction KD. In all cases, we can see that the cross sections calculated with the coupled-cluster optical potential are larger than the predictions obtained with the KD potential.

#### IV. CONCLUSIONS

In this paper we constructed microscopic nuclear optical potentials by combining the Green's function approach with the coupled-cluster method at the singles and doubles truncation level. We used an analytical continuation in the complex-energy plane, based on a complex Berggren basis, to compute the Green's function. The Dyson equation was then inverted to obtain the optical potential. We showed applications for  $^{40}\text{Ca}$  and  $^{48}\text{Ca}$  with the chiral  $NN$  and  $3NF$  interaction  $\text{NNLO}_{\text{sat}}$ . The choice of this interaction was motivated by the fact that it allows for a good description of masses and radii in a wide mass-range and, furthermore, it reproduces the charge radii of  $^{40}\text{Ca}$  and  $^{48}\text{Ca}$ . First we showed results for the optical potentials associated with the bound states in  $^{41}\text{Ca}$  and  $^{49}\text{Ca}$  and then presented applications to the neutron scattering. We also showed, for comparison, the results for neutron scattering obtained with the chiral  $NN$  interaction  $\text{NNLO}_{\text{opt}}$ , and with the phenomenolog-



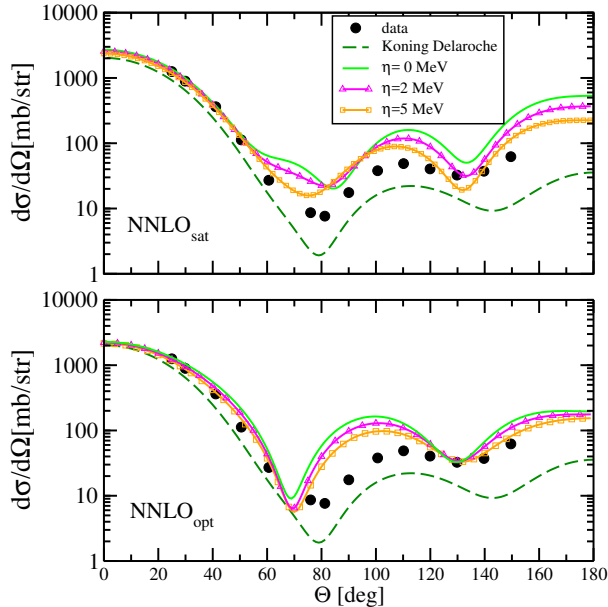


FIG. 10. (Color online) Differential elastic cross section for  $^{48}\text{Ca}(n,n)^{48}\text{Ca}$  at 7.81 MeV calculated with the  $\text{NNLO}_{\text{sat}}$  (top) and  $\text{NNLO}_{\text{opt}}$  (bottom) interactions. Calculations are shown for  $\eta = 0, 2, 5$  MeV. Results obtained using the KD potential are shown for comparison. Data points are taken from [58].

ical Koning-Delaroche potential. We have seen that the overall form of the scattering cross section is reproduced for both nuclei at several scattering energies. At this level of truncation, the absorption is practically negligible which points to a lack of many-body correlations in the wave functions of the coupled-cluster method at the singles and doubles approximation level. We showed that, by increasing the parameter  $\eta$  in the Green's func-

tion, results can be somewhat improved.

This work can be extended in several directions. We plan to consider higher-order correlations in our coupled-cluster Green's function calculations as was recently done for the dipole response of  $^{48}\text{Ca}$  [65], and excited states in  $^{101}\text{Sn}$  [8]. The first step will be to include iterative triples excitations in the ground-state, and investigate the impact of these correlations on the absorptive character of the calculated optical potential. It could also be interesting to investigate optical potentials constructed by starting with the singles and doubles coupled-cluster Green's function potential and add an *ad hoc* polarization terms which would effectively account for the missing physics (such as collective excitations and formation of compound nucleus) at that level of truncations.

#### ACKNOWLEDGMENTS

We thank K. Hebeler for providing us with matrix elements in Jacobi coordinates for the  $\text{NNN}$  interaction at next-to-next-to-leading order. We acknowledge beneficial discussions with Willem Dickhoff, Charlotte Elster, Heiko Hergert and Grégory Potel. This work was supported by the National Science Foundation under Grant PHY-1403906, the Department of Energy under Contract No. DE-FG52-08NA28552, by the Office of Science, U.S. Department of Energy under Award Number DE-SC0013365 and by the Office of Nuclear Physics, U.S. Department of Energy, under Grants DE-SC0008499 (SciDAC-3 NUCLEI), DE-SC0018223 (SciDAC-4 NUCLEI), the Field Work Proposal ERKBP57 and ERKBP72 at Oak Ridge National Laboratory (ORNL). An award of computer time was provided by the Institute for Cyber-Enabled Research at Michigan State University and part of this research used resources of the Oak Ridge Leadership Computing Facility located at ORNL, which is supported by the Office of Science of the Department of Energy under Contract No. DE-AC05-00OR22725.

[1] <http://www.nupecc.org/index.php?display=lrp2016/main>.  
[2] G. Bollen, "Frib - facility for rare isotope beams," in *AIP Conference Proceedings*, Vol. 1224 (2010) pp. 432–441.  
[3] O. Kester and H. Stöcker, *FAIR project at GSI* (World Scientific Publishing Co, 2016).  
[4] Ian J. Thompson and Filomena M. Nunes, *Nuclear Reactions for Astrophysics* (Cambridge University Press, 2009).  
[5] U. Van Kolck, "Effective field theory of nuclear forces," *Progress in Particle and Nuclear Physics* **43**, 337 – 418 (1999).  
[6] E. Epelbaum, H.-W. Hammer, and Ulf-G. Meißner, "Modern theory of nuclear forces," *Rev. Mod. Phys.* **81**, 1773–1825 (2009).  
[7] R. Machleidt and D.R. Entem, "Chiral effective field theory and nuclear forces," *Physics Reports* **503**, 1 – 75

(2011).  
[8] T. D. Morris, J. Simonis, S. R. Stroberg, C. Stumpf, G. Hagen, J. D. Holt, G. R. Jansen, T. Papenbrock, R. Roth, and A. Schwenk, "Structure of the lightest tin isotopes," *Phys. Rev. Lett.* **120**, 152503 (2018).  
[9] Bogdan Mihaila and Jochen H. Heisenberg, "Microscopic Calculation of the Inclusive Electron Scattering Structure Function in  $^{16}\text{O}$ ," *Phys. Rev. Lett.* **84**, 1403–1406 (2000).  
[10] D. J. Dean and M. Hjorth-Jensen, "Coupled-cluster approach to nuclear physics," *Phys. Rev. C* **69**, 054320 (2004).  
[11] W.H. Dickhoff and C. Barbieri, "Self-consistent green's function method for nuclei and nuclear matter," *Progress in Particle and Nuclear Physics* **52**, 377 – 496 (2004).  
[12] G. Hagen, T. Papenbrock, D. J. Dean, and M. Hjorth-Jensen, "Medium-mass nuclei from chiral nucleon-nucleon interactions," *Phys. Rev. Lett.* **101**, 092502

- (2008).
- [13] G. Hagen, T. Papenbrock, D. J. Dean, and M. Hjorth-Jensen, “*Ab initio* coupled-cluster approach to nuclear structure with modern nucleon-nucleon interactions,” *Phys. Rev. C* **82**, 034330 (2010).
- [14] K. Tsukiyama, S. K. Bogner, and A. Schwenk, “In-Medium Similarity Renormalization Group For Nuclei,” *Phys. Rev. Lett.* **106**, 222502 (2011).
- [15] Robert Roth, Sven Binder, Klaus Vobig, Angelo Calci, Joachim Langhammer, and Petr Navrátil, “Medium-Mass Nuclei with Normal-Ordered Chiral  $NN+3N$  Interactions,” *Phys. Rev. Lett.* **109**, 052501 (2012).
- [16] H. Hergert, S. K. Bogner, S. Binder, A. Calci, J. Langhammer, R. Roth, and A. Schwenk, “In-medium similarity renormalization group with chiral two- plus three-nucleon interactions,” *Phys. Rev. C* **87**, 034307 (2013).
- [17] V. Somà, A. Cipollone, C. Barbieri, P. Navrátil, and T. Duguet, “Chiral two- and three-nucleon forces along medium-mass isotope chains,” *Phys. Rev. C* **89**, 061301 (2014).
- [18] Sven Binder, Piotr Piecuch, Angelo Calci, Joachim Langhammer, Petr Navrátil, and Robert Roth, “Extension of coupled-cluster theory with a noniterative treatment of connected triply excited clusters to three-body hamiltonians,” *Phys. Rev. C* **88**, 054319 (2013).
- [19] T. A. Lähde, E. Epelbaum, H. Krebs, D. Lee, U.-G. Meißner, and G. Rupak, “Lattice effective field theory for medium-mass nuclei,” *Phys. Lett. B* **732**, 110 – 115 (2014).
- [20] Kenneth M. Nollett, Steven C. Pieper, R. B. Wiringa, J. Carlson, and G. M. Hale, “Quantum Monte Carlo Calculations of Neutron- $\alpha$  Scattering,” *Phys. Rev. Lett.* **99**, 022502 (2007).
- [21] S. Quaglioni and P. Navrátil, “*Ab Initio* many-body calculations of  $n-^3\text{H}$ ,  $n-^4\text{He}$ ,  $p-^3,^4\text{He}$ , and  $n-^{10}\text{Be}$  scattering,” *Phys. Rev. Lett.* **101**, 092501 (2008).
- [22] Guillaume Hupin, Joachim Langhammer, Petr Navrátil, Sofia Quaglioni, Angelo Calci, and Robert Roth, “*Ab initio* many-body calculations of nucleon- $^4\text{He}$  scattering with three-nucleon forces,” *Phys. Rev. C* **88**, 054622 (2013).
- [23] S. Elhatisari, D. Lee, G. Rupak, E. Epelbaum, H. Krebs, T. A. Lähde, T. Luu, and U.-G. Meißner, “*Ab initio* alpha-alpha scattering,” *Nature* **528**, 111–114 (2015).
- [24] I. A. Mazur, A. M. Shirokov, A. I. Mazur, and J. P. Vary, “Description of resonant states in the shell model,” *ArXiv e-prints* (2015), arXiv:1512.03983 [nucl-th].
- [25] P. Navrátil and S. Quaglioni, “*Ab Initio* many-body calculations of the  $^3\text{H}(d,n)^4\text{He}$  and  $^3\text{He}(d,p)^4\text{He}$  fusion reactions,” *Phys. Rev. Lett.* **108**, 042503 (2012).
- [26] Doron Gazit, Sonia Bacca, Nir Barnea, Winfried Leidemann, and Giuseppina Orlandini, “Photoabsorption on  $^4\text{He}$  with a realistic nuclear force,” *Phys. Rev. Lett.* **96**, 112301 (2006).
- [27] V D Efron, W Leidemann, G Orlandini, and N Barnea, “The lorentz integral transform (lit) method and its applications to perturbation-induced reactions,” *Journal of Physics G: Nuclear and Particle Physics* **34**, R459 (2007).
- [28] L. Girlanda, A. Kievsky, L. E. Marcucci, S. Pastore, R. Schiavilla, and M. Viviani, “Thermal neutron captures on  $d$  and  $^3\text{He}$ ,” *Phys. Rev. Lett.* **105**, 232502 (2010).
- [29] L. E. Marcucci, R. Schiavilla, and M. Viviani, “Proton-proton weak capture in chiral effective field theory,” *Phys. Rev. Lett.* **110**, 192503 (2013).
- [30] P. Navratil, S. Quaglioni, G. Hupin, C. Romero-Redondo, and A. Calci, “Unified *ab initio* approaches to nuclear structure and reactions,” *ArXiv e-prints* (2016), arXiv:1601.03765 [nucl-th].
- [31] G. Hagen and N. Michel, “Elastic proton scattering of medium mass nuclei from coupled-cluster theory,” *Phys. Rev. C* **86**, 021602 (2012).
- [32] S. Bacca, N. Barnea, G. Hagen, M. Miorelli, G. Orlandini, and T. Papenbrock, “Giant and pigmy dipole resonances in  $^4\text{He}$ ,  $^{16,22}\text{O}$ , and  $^{40}\text{Ca}$  from chiral nucleon-nucleon interactions,” *Phys. Rev. C* **90**, 064619 (2014).
- [33] S. Bacca and S. Pastore, “Electromagnetic reactions on light nuclei,” *J. Phys. G: Nucl. Part. Phys.* **41**, 123002 (2014).
- [34] A. Idini, C. Barbieri, and P. Navrátil, “*Ab Initio* Optical Potentials and Nucleon Scattering on Medium Mass Nuclei,” *Acta Physica Polonica B* **48**, 273 (2017), arXiv:1612.01478 [nucl-th].
- [35] J. Rotureau, P. Danielewicz, G. Hagen, F. Nunes, and T. Papenbrock, “Optical potential from first principles,” *Phys. Rev.* **C95**, 024315 (2017).
- [36] C. Barbieri and B. K. Jennings, “Nucleon-nucleus optical potential in the particle-hole approach,” *Phys. Rev. C* **72**, 014613 (2005).
- [37] M. H. Mahzoon, R.J.Charity, W.H.Dickhoff, H.Dussan, and S.J.Waldecker, *Phys. Rev. Lett.* **112**, 162503 (2014).
- [38] Carlo Barbieri and Arianna Carbone, “Self-consistent green’s function approaches,” in *An Advanced Course in Computational Nuclear Physics: Bridging the Scales from Quarks to Neutron Stars*, edited by Morten Hjorth-Jensen, Maria Paola Lombardo, and Ubirajara van Kolck (Springer International Publishing, Cham, 2017) pp. 571–644.
- [39] H. Kümmel, K. H. Lührmann, and J. G. Zabolitzky, “Many-fermion theory in expS- (or coupled cluster) form,” *Physics Reports* **36**, 1 – 63 (1978).
- [40] R. F. Bishop, “An overview of coupled cluster theory and its applications in physics,” *Theoretical Chemistry Accounts: Theory, Computation, and Modeling (Theoretica Chimica Acta)* **80**, 95–148 (1991), 10.1007/BF01119617.
- [41] Rodney J. Bartlett and Monika Musiał, “Coupled-cluster theory in quantum chemistry,” *Rev. Mod. Phys.* **79**, 291–352 (2007).
- [42] Sven Binder, Joachim Langhammer, Angelo Calci, and Robert Roth, “*Ab initio* path to heavy nuclei,” *Physics Letters B* **736**, 119 – 123 (2014).
- [43] G. Hagen, T. Papenbrock, M. Hjorth-Jensen, and D. J. Dean, “Coupled-cluster computations of atomic nuclei,” *Rep. Prog. Phys.* **77**, 096302 (2014).
- [44] Elbio Dagotto, “Correlated electrons in high-temperature superconductors,” *Rev. Mod. Phys.* **66**, 763–840 (1994).
- [45] Karen A. Hallberg, “Density-matrix algorithm for the calculation of dynamical properties of low-dimensional systems,” *Phys. Rev. B* **52**, R9827–R9830 (1995).
- [46] Wick C. Haxton, Kenneth M. Nollett, and Kathryn M. Zurek, “Piecewise moments method: Generalized lanczos technique for nuclear response surfaces,” *Phys. Rev. C* **72**, 065501 (2005).
- [47] Tore Berggren, “On the use of resonant states in eigenfunction expansions of scattering and reaction amplitudes,” *Nuclear Physics A* **109**, 265 – 287 (1968).
- [48] N. Michel, W. Nazarewicz, M. Płoszajczak, and K. Bennecheur, “Gamow shell model description of neutron-rich nuclei,” *Phys. Rev. Lett.* **89**, 042502 (2002).

- [49] R. Id Betan, R. J. Liotta, N. Sandulescu, and T. Vertse, “Two-particle resonant states in a many-body mean field,” *Phys. Rev. Lett.* **89**, 042501 (2002).
- [50] G. Hagen, J. S. Vaagen, and M. Hjorth-Jensen, “The contour deformation method in momentum space, applied to subatomic physics,” *Journal of Physics A: Mathematical and General* **37**, 8991 (2004).
- [51] G. Hagen and J. S. Vaagen, “Study of resonant structures in a deformed mean field by the contour deformation method in momentum space,” *Phys. Rev. C* **73**, 034321 (2006).
- [52] A. Ekström, G. R. Jansen, K. A. Wendt, G. Hagen, T. Papenbrock, B. D. Carlsson, C. Forssén, M. Hjorth-Jensen, P. Navrátil, and W. Nazarewicz, “Accurate nuclear radii and binding energies from a chiral interaction,” *Phys. Rev. C* **91**, 051301 (2015).
- [53] G. Hagen, A. Ekström, C. Forssén, G. R. Jansen, W. Nazarewicz, T. Papenbrock, K. A. Wendt, S. Bacca, N. Barnea, B. Carlsson, C. Drischler, K. Hebeler, M. Hjorth-Jensen, M. Miorelli, G. Orlandini, A. Schwenk, and J. Simonis, “Neutron and weak-charge distributions of the  $^{48}\text{Ca}$  nucleus,” *Nature Physics* **12**, 186 (2016).
- [54] R. F. Garcia Ruiz, M. L. Bissell, K. Blaum, A. Ekström, N. Frömmgen, G. Hagen, M. Hammen, K. Hebeler, J. D. Holt, G. R. Jansen, M. Kowalska, K. Kreim, W. Nazarewicz, R. Neugart, G. Neyens, W. Nörtershäuser, T. Papenbrock, J. Papuga, A. Schwenk, J. Simonis, K. A. Wendt, and D. T. Yordanov, “Unexpectedly large charge radii of neutron-rich calcium isotopes,” *Nature Physics* (2016), 10.1038/nphys3645, 1602.07906.
- [55] V. Lapoux, V. Somà, C. Barbieri, H. Hergert, J. D. Holt, and S. R. Stroberg, “Radii and binding energies in oxygen isotopes: A challenge for nuclear forces,” *Phys. Rev. Lett.* **117**, 052501 (2016).
- [56] T. Duguet, V. Somà, S. Lecluse, C. Barbieri, and P. Navrátil, “Ab initio calculation of the potential bubble nucleus  $^{34}\text{Si}$ ,” *Phys. Rev. C* **95**, 034319 (2017).
- [57] A. Ekström, G. Baardsen, C. Forssén, G. Hagen, M. Hjorth-Jensen, G. R. Jansen, R. Machleidt, W. Nazarewicz, T. Papenbrock, J. Sarich, and S. M. Wild, “Optimized chiral nucleon-nucleon interaction at next-to-next-to-leading order,” *Phys. Rev. Lett.* **110**, 192502 (2013).
- [58] A.J. Koning and J.P. Delaroche, “Local and global nucleon optical models from 1 keV to 200 MeV,” *Nuclear Physics A* **713**, 231 – 310 (2003).
- [59] F. Capuzzi and C. Mahaux, “Projection operator approach to the self-energy,” *Annals of Physics* **245**, 147 – 208 (1996).
- [60] W. H. Dickhoff and D. Van Neck, *Many-Body Theory Exposed!* (World Scientific, Singapore, 2007).
- [61] J. R. Gour, P. Piecuch, M. Hjorth-Jensen, M. Włoch, and D. J. Dean, “Coupled-cluster calculations for valence systems around  $^{16}\text{O}$ ,” *Phys. Rev. C* **74**, 024310 (2006).
- [62] G. Hagen, M. Hjorth-Jensen, G. R. Jansen, and T. Papenbrock, “Emergent properties of nuclei from ab initio coupled-cluster calculations,” *Physica Scripta* **91**, 063006 (2016).
- [63] R. C. Johnson, “Translation invariance and antisymmetry in the theory of the nucleon optical model,” *Phys. Rev. C* **95**, 064610 (2017).
- [64] G. E. Mitchell, A. Richter, and H. A. Weidenmüller, “Random matrices and chaos in nuclear physics: Nuclear reactions,” *Rev. Mod. Phys.* **82**, 2845–2901 (2010).
- [65] M. Miorelli, S. Bacca, G. Hagen, and T. Papenbrock, “Computing the dipole polarizability of  $^{48}\text{Ca}$  with increased precision,” *Phys. Rev. C* **98**, 014324 (2018).